In-situ optical spectroscopy for monitoring plasma-assisted formation of lanthanide metal-organic frameworks

Xiaohui Wen,[a] Yanju Luo,[a] Yujia Deng,[c] Xiaoliang Zeng,[d] Yunfei Tian,[a] Juan He[a*] and Xiandeng Hou[a,b*]

[a]*Analytical & Testing Center, Sichuan University, Chengdu, Sichuan 610064, China;*

[b]*College of Chemistry, Sichuan University, Chengdu, Sichuan 610064, China.*

[c]*College of Chemistry and Chemical Engineering, China West Normal University, Nanchong, Sichuan 637009, China*

[d]*State Grid Sichuan Electric Power Research Institute, Chengdu, Sichuan 610041, China.*

* To whom correspondence should be addressed. E-mails: hejuan1117@scu.edu.cn; houxd@scu.edu.cn

1. Experimental section

1.1 Reagents and Chemicals

All chemicals in this work were obtained as analytical grade and used without further purification. Terbium(III) nitrate hexahydrate ($Tb(NO_3)_3 \cdot 6H_2O$) and europium(III) nitrate hexahydrate ($Eu(NO_3)_3 \cdot 6H_2O$) were purchased from the Energy Chemical (Shanghai, China). 1,3,5-Benzenetricarboxylic acid (H_3BTC) and 1,4-dicarboxybenzene (H_2BDC) were purchased from the Aladdin Reagent Co.Ltd. (Shanghai, China). *N*, *N*-dimethylformamide (DMF) and ethanol were purchased from Kelong Chemical Reagent Co. Ltd. (Chengdu, China).

1.2 Instrumentation

The powder X-ray diffraction (PXRD) patterns were obtained from an X'Pert Pro MPD (Philips, Netherlands) X-ray diffraction spectrometer using Cu_{ka} radiation. The scanning electron microscopy (SEM) images were recorded with a JEOL JSM-7500F scanning electron microscope at 30.0 kV. The photoluminescence (PL) spectra were collected with a Fluorolog-3 spectrometer (Horiba Jobin Yvon, France) using a 350 nm optical filter with excitation wavelength at 302 nm. The nitrogen (N_2) adsorption-desorption isotherms were obtained using the Brunauer-Emmett-Teller (BET) method on surface area and porosity analyzer Micromeritics ASAP 2460 (4356 Communications Dr. Norcross, GA 30093-2901, USA) at 77 K. A Uwave-1000 microwave reactor for the synthesis of Tb(BDC) was purchased from Sineo Microwave Chemistry Technology Co. Ltd. (Shanghai, China). CCD spectrometer (Maya 2000 PRO, 25 μm slit, 399-842 nm) was purchased from American Ocean Optics. A portable ultraviolet excitation light source with a 302 nm lamp was purchased from Shanghai Chi Tang Instrument Co., Ltd.

1.3 Experimental device for synthesis and monitoring

The DBD-based reactor was composed of an open concentric quartz cylinder tube: a tungsten rod, which was embedded inside an inner cylinder, acted as the internal electrode; and a Cu wire, surrounding the outside of the larger quartz tube, was used as the outer electrode. When the power was on, the reaction began. The spectral monitoring device included a CCD-based miniature spectrometer, connected to an optical fiber. The optical fiber was placed on the top side of the DBD reactor for real-time collection of luminescence spectra of the reaction mixture in the DBD. A portable ultraviolet excitation source was placed at an angle of 90° to the detector.

1.4 Synthesis

***In-situ* syntheses.** Synthesis of Tb(BTC), Eu(BTC) and Tb(BDC) for *in-situ* monitoring were carried out under mild conditions by applying an electric power for dielectric barrier discharge (DBD). For synthesis of Tb(BTC), $Tb(NO_3)_3 \cdot 6H_2O$ (23 mg, 0.005 mmol) and $H_3(BTC)$ (10 mg, 0.005 mmol) were dissolved in 6 mL DMF. For synthesis of Eu(BTC), $Eu(NO_3)_3 \cdot 6H_2O$ (22 mg, 0.005mmol) and $H_3(BTC)$ (10 mg, 0.005 mmol) were dissolved in 6 mL DMF. For synthesis of Tb(BDC), $Tb(NO_3)_3 \cdot 6H_2O$ (23 mg, 0.005mmol) and $H_2(BDC)$ (11 mg, 0.005 mmol) were dissolved in 6 mL DMF. These mixed solutions were then added to the DBD-based reactor. The materials were synthesized when a liquid-phase DBD plasma was generated under specific conditions (28 V and 1.30 A). For confirming the formation of the products, the products at different reaction time were removed from the DBD-based vessel, centrifuged and thoroughly rinsed three times with DMF and ethanol or water respectively. The obtained product was dried (under vacuum) at 80°C for 8 h for *ex-situ* XRD, SEM and luminescence analysis.

***Ex-situ* syntheses.** The Tb(BTC) synthesized here was obtained according to a previously reported solvothermal method with a slightly modified procedure.[1] A solution of H_3BTC (20 mg, 0.10 mmol), $Tb(NO_3)_3 \cdot 6H_2O$ (120 mg, 0.28 mmol) in a solvent containing DMF (4 mL), ethanol (4 mL), and H_2O (3.2 mL) was heated in a sealed vial at 80°C for 24 h and then cooled to room temperature. The obtained products centrifuged and thoroughly rinsed three times with DMF and ethanol or water respectively, then dried (under vacuum) at 80°C for 8 h for *ex-situ* XRD and luminescence analysis.

The Eu(BTC) synthesized here was obtained according to a previously reported solvothermal method.[2] A solution of H_3BTC (15.6 mg, 0.074 mmol) and $Eu(NO_3)_3 \cdot 6H_2O$ (33.1 mg, 0.074 mmol) in a solvent containing DMF (3 mL), ethanol (3 mL), and H_2O (2 mL) was heated in a sealed vial (20 mL) at 80°C for 24 h.

The Tb(BDC) synthesized here was obtained according to a previously reported microwave method.[3] A solution of $Tb(NO_3)_3 \cdot 5H_2O$ (113 mg, 0.25 mmol) and H_2BDC (42 mg, 0.25 mmol) in a solvent containing DMF (50 mL), which was heated in the microwave reactor under autogenous pressure at 120°C, 500 W for 1 h.
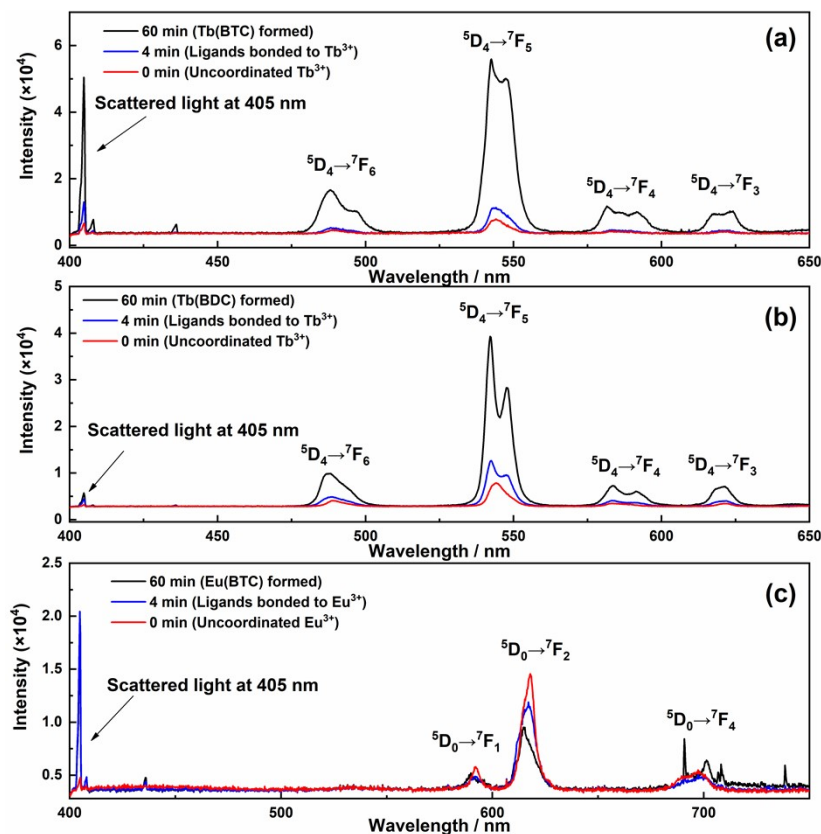
2. Results and discussion

Figure S1. Comparison of *in-situ* luminescence and scattering spectra of Tb(BTC), Tb(BDC) and Eu(BTC) recorded at t = 0 min, t = 4 min and t = 60 min.

The portable UV Lamp used in our work is actually a medium-pressure mercury lamp, which is filled with mercury vapor and argon in the central discharge tube, and coated with special fluorescent phosphors material in the inner surface. When mercury and argon vapor are ionized and excited by energy source, these excited states are inherently unstable, and they will revert to their original ground-state orbitals and emit the five main UV radiations at 254 nm, 313 nm, 366 nm (i-line), 405 nm (h-line) and 436 nm (g-line), and a large number of other radiation lines in the visible and infrared region. Therefore, the sharp and multiple emission lines including sharp peak at 405 nm originate from excited atomic mercury, while the wide band around 302 nm originates from the special fluorescent material (Figure S2).
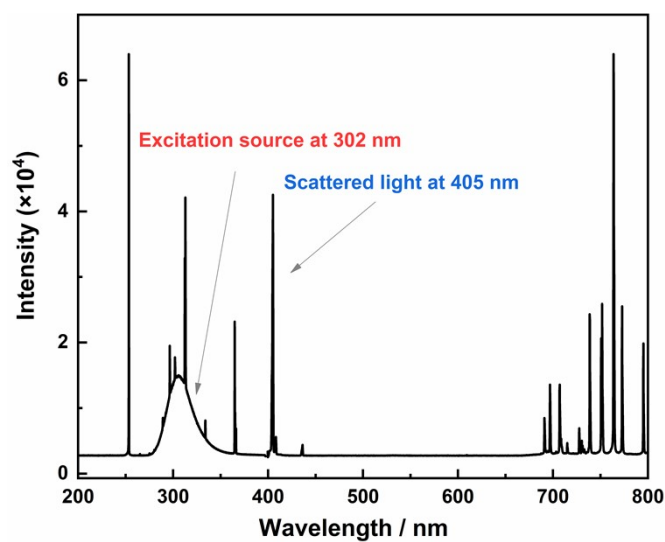
Figure S2. Background signal of UV light. The sharp and multiple emission lines originate from excited atomic mercury vapor, while the wide band around 302 nm originates from the special fluorescent material coated in the lamp.
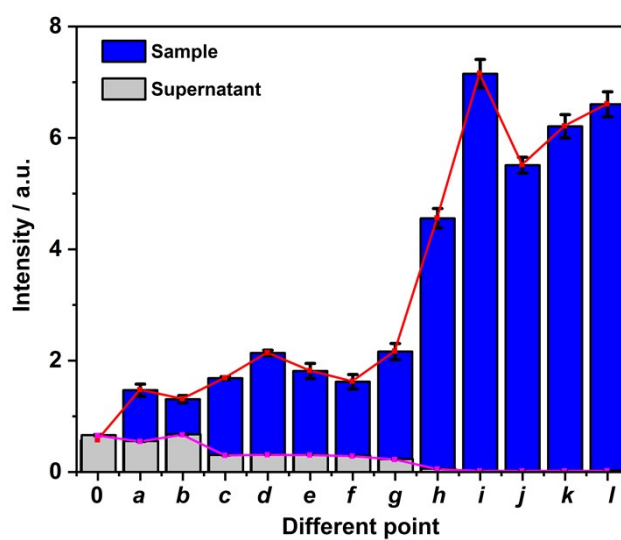

Figure S3. Comparison of the luminescence intensity of sample and supernatant recorded at different point using a Fluorolog-3 spectrometer.
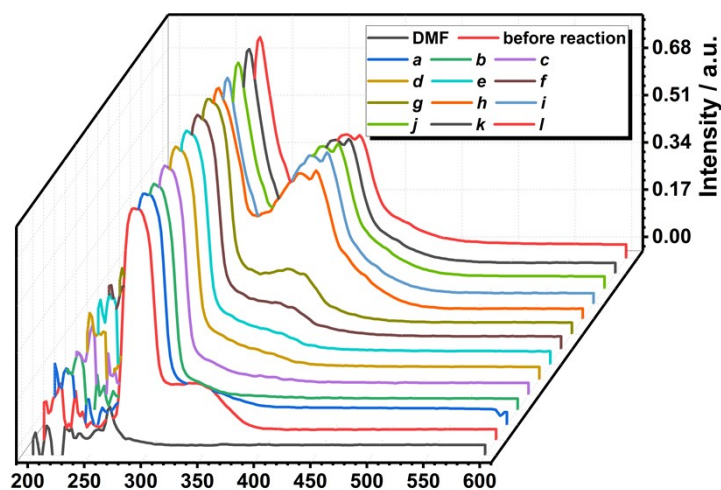
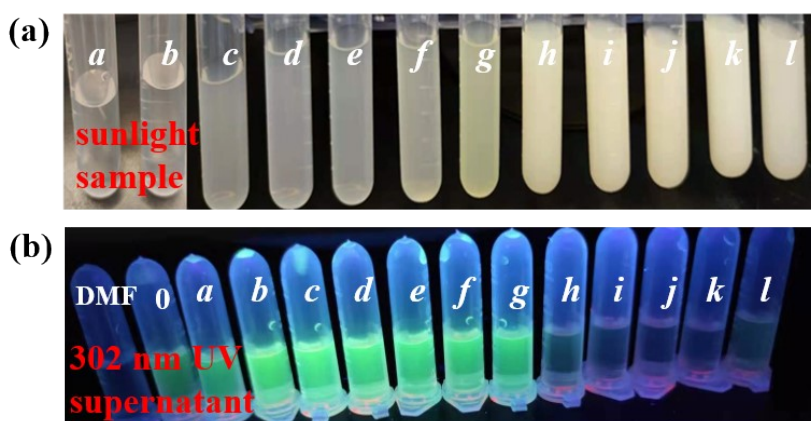**Figure S4**. UV-Vis absorption spectrum of supernatant at different points.

Figure S5. Appearances of Tb(BTC) at different points.

At the beginning of crystal growth, the coordination reaction between the H_3BTC ligand and Tb^{3+} ions just happened to generate few nanosized primary particles of Tb(BTC). A colloid solution gradually formed with the increase of these nanosized primary particles as the reaction progressed. These primary particles were too small to be visible by naked eyes especially for point a. The appearance of Tb(BTC) at points a and b in Figure S5a also show that the solution was clear and no product was visible to the naked eyes. It was tried to collect these nanosized primary particles, but unfortunately, due to the ultra-small size and ultra-low concentration of particles, it is impossible to conduct IR spectra analysis at points a and b (Figure S6). Although IR analysis failed, SEM and TEM were successfully applied for their characterization, which also helped to gain understanding of the MOFs crystal growth.
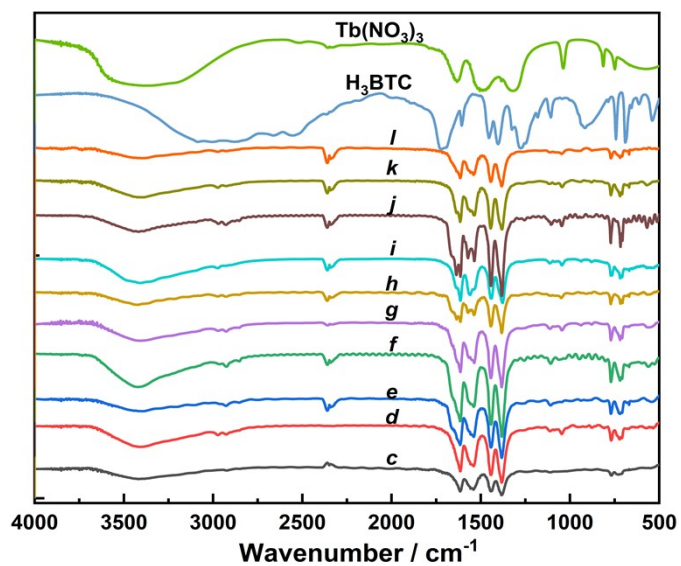
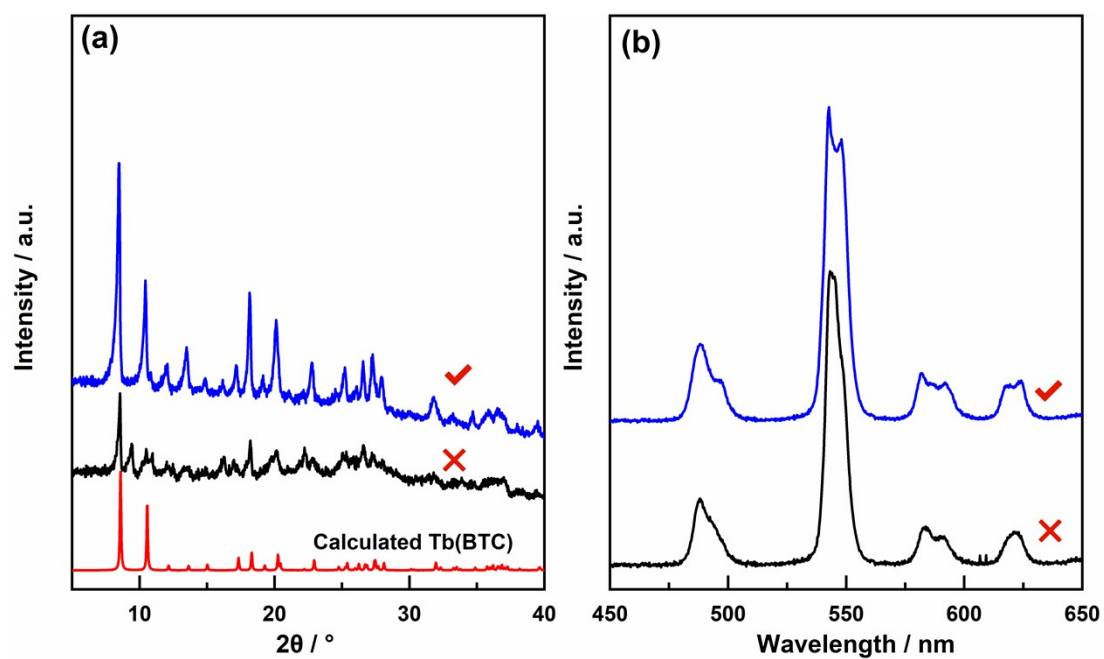**Figure S6**. Fourier transform infrared spectra of Tb(BTC) at different points.

Figure S7. (a) The XRD and (b) Luminescence spectra of Tb(BTC) synthesized successfully and unsuccessfully, respectively.
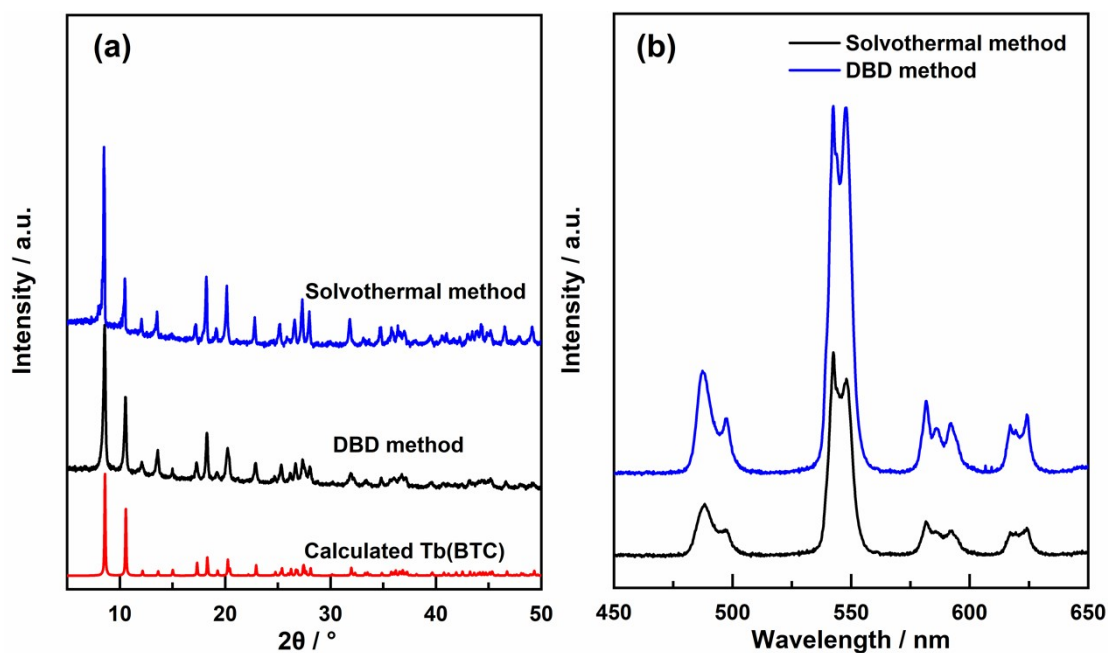
Figure S8. (a) The XRD and (b) Luminescence spectra of Tb(BTC) synthesized by DBD and solvothermal methods, respectively.
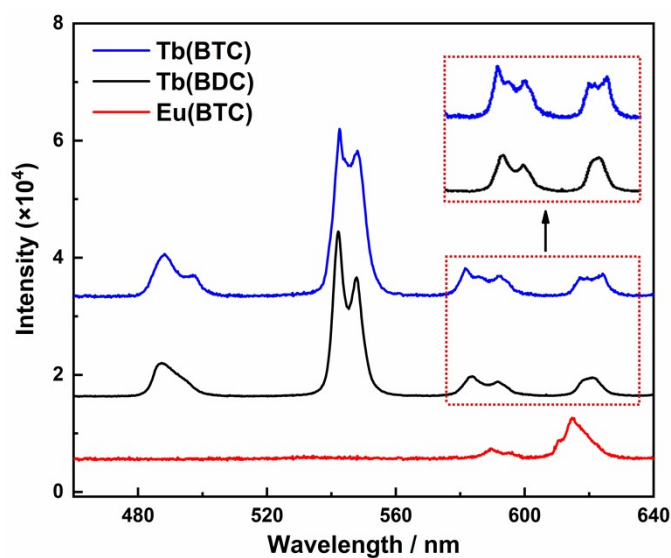

Figure S9. The fine structure comparison between Tb(BTC), Tb(BDC) and Eu(BTC).

Detection of formation of Tb(BDC) and Eu(BTC) by Luminescence

According to the foregoing statement, the appearance of the fine-structure can determine the synthesis time of good crystallinity of products. Furthermore, to confirm that the fine structure of the compounds synthesized by DBD method arises from Tb(BDC) indeed, we then synthesized Tb(BDC) by conventional microwave method and subsequently measured its luminesence spectra. As expected, the fine structure of Tb(BDC) synthesized by microwave

and DBD methods are highly consistent (Figure S10), indicating that the fine-structure of the compounds synthesized by DBD is derived from Tb(BDC).
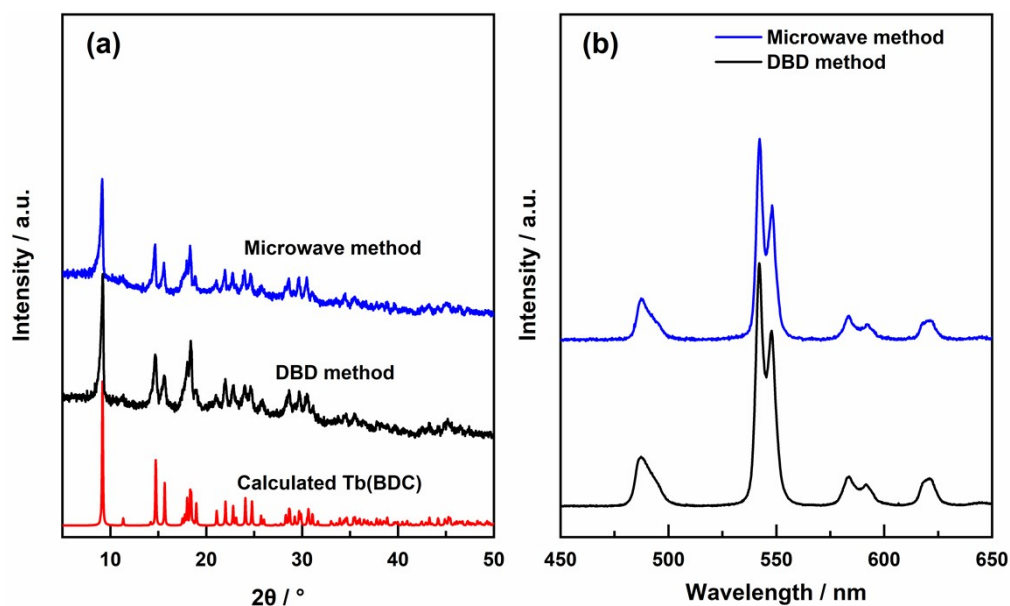

Figure S10. (a) The XRD and (b) Luminescence spectra of Tb(BDC) synthesized by DBD and solvothermal methods, respectively.
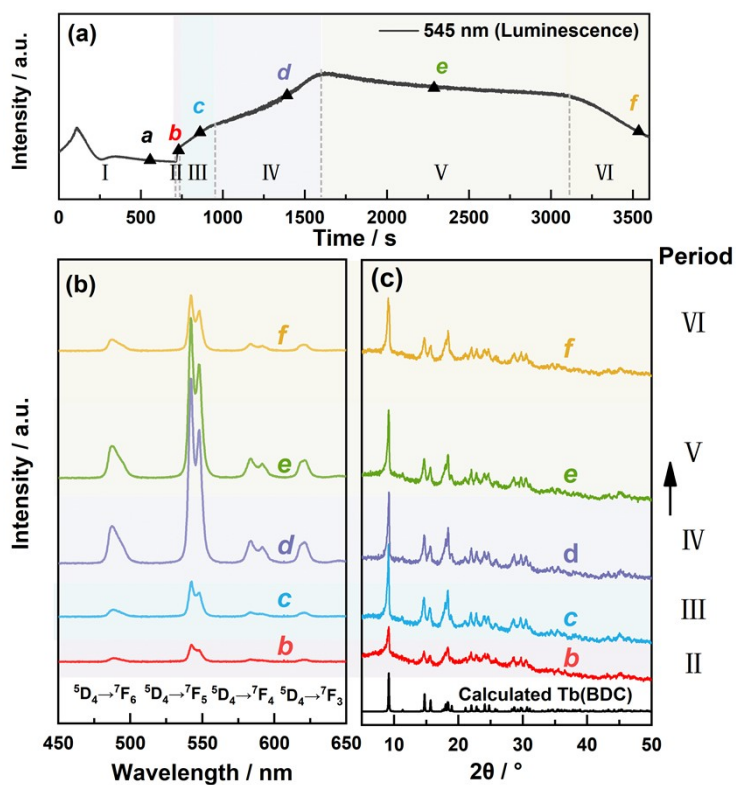

Figure S11. *In-situ* luminescence measurements during the formation of Tb(BDC). (a) Time dependence of emission intensity at 544 nm (λ_{ex} = 302 nm); (b) *In-situ* luminescence spectra; (c) *Ex-situ* XRD. I:

Nano-sized primary particles; II: Generation of products; III,IV: Growth of products; V: End of reaction; VI: Fragmentation of products.

Fluorolog-3 spectrometer was applied to characterize the luminescence spectra of Eu(BTC) synthesized by solvothermal method and DBD method respectively (Figure S12). The appearance of the two main peaks at 590 nm and 618 nm were attributed to $^5D_0{\rightarrow}^7F_1$, $^5D_0{\rightarrow}^7F_2$ electronic transitions of Eu^{3+}, and the generation of the fine structure in the main peaks was attributed to the splitting of the coordination field. We found that the fine structure of Eu(BTC) obtained by the two methods are slightly different, the fine structure obtained by the solvothermal method had more tiny peaks. Because the materials synthesized by solvothermal method own a better crystallinity and higher emission intensity, the fine-structure appears more completely. Therefore, the fine-structure appearred by DBD method also can be used to determine the synthesis of good crystallinity of products.
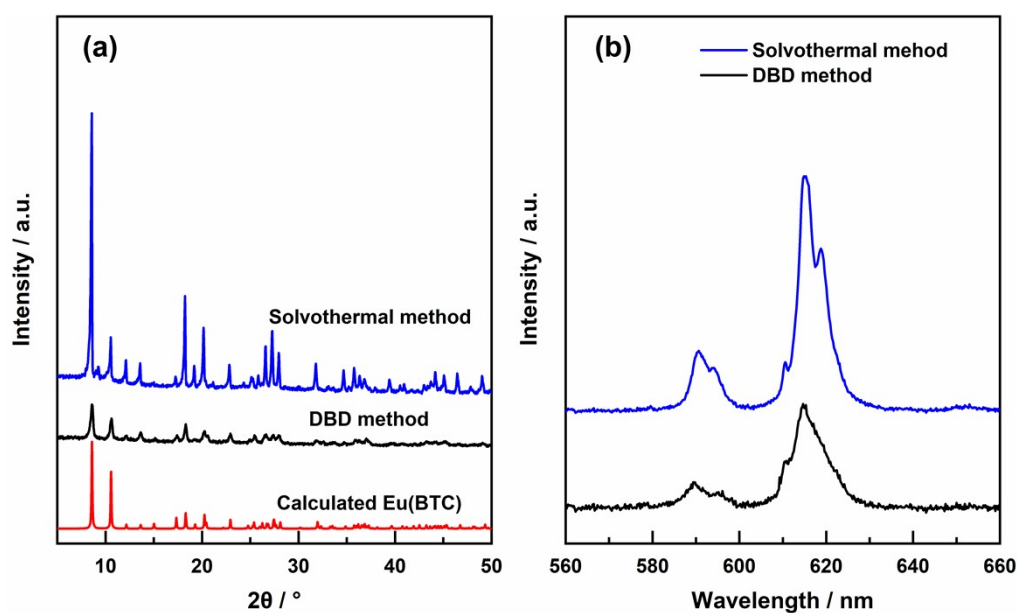

Figure S12. (a) The XRD and (b) Luminescence spectra of Eu(BTC) synthesized by DBD and solvothermal methods, respectively.
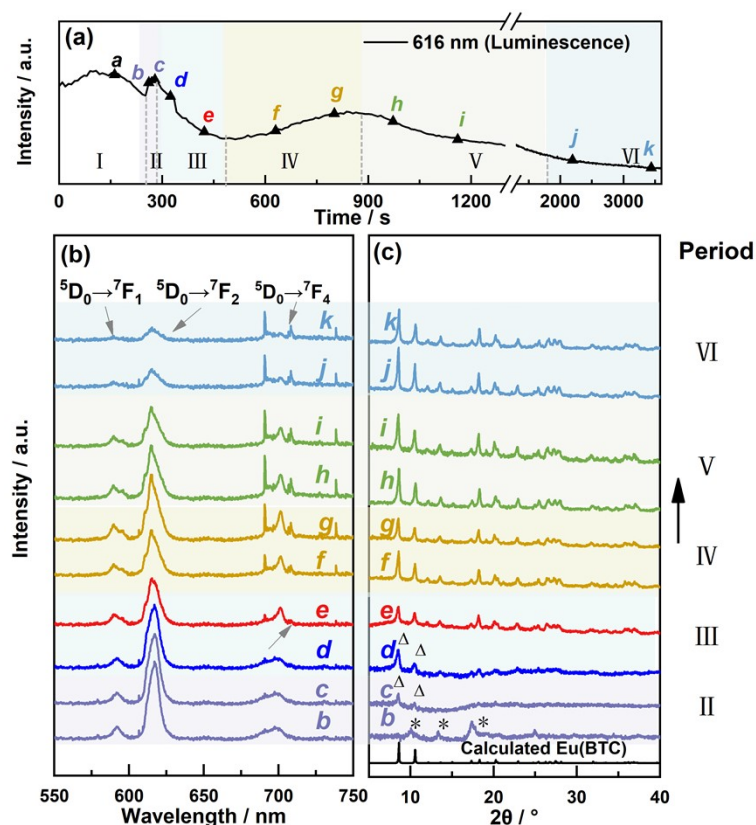
Figure S13. *In-situ* luminescence measurements during the formation of Eu(BTC). (a) Time dependence of emission intensity at 616 nm (λ_{ex} = 302 nm); (b) *In-situ* luminescence spectra; (c) *Ex-situ* XRD. I: Nano-sized primary particles; II: Intermediates; III: Generation of products; IV: Growth of products; V: End of reaction; VI: Fragmentation of products. * and △: The characteristic diffraction peaks of starting intermediates and Eu(BTC), respectively.

Firstly, the sharp peak at 405 nm is indeed generated by the UV light. Because the CCD detector is placed 90 degrees perpendicular to the light source, only extremely faint light at 405 nm is scattered into the CCD and observed when the solution is clear and transparent. Thus, the intensity of 405 nm peak is unchanged when the solution remains clear (Figure S13). As the turbidity of the solution increases along with the generation of solid product, more and more background light at 405 nm is scattered into the CCD detector, resulting in the dramatical increasing of the peak intensity at 405 nm. Therefore, the variation of light intensity at 405nm can reflect the change of scattered light caused by the formation of the product. Besides, the 365 nm UV light instead of 302 nm UV light can also be scattered into the CCD detector when the solution become turbid (Figure S14), indicating that the 405 nm sharp peak is not generated by the materials. At the same time, the excitation spectrum of the Tb(BTC) is between 250-350 nm (Figure S15), illustrating that the light at 405 nm cannot be absorbed. Therefore, the 405 nm sharp peak can be used as ideal and suitable scattering light source.
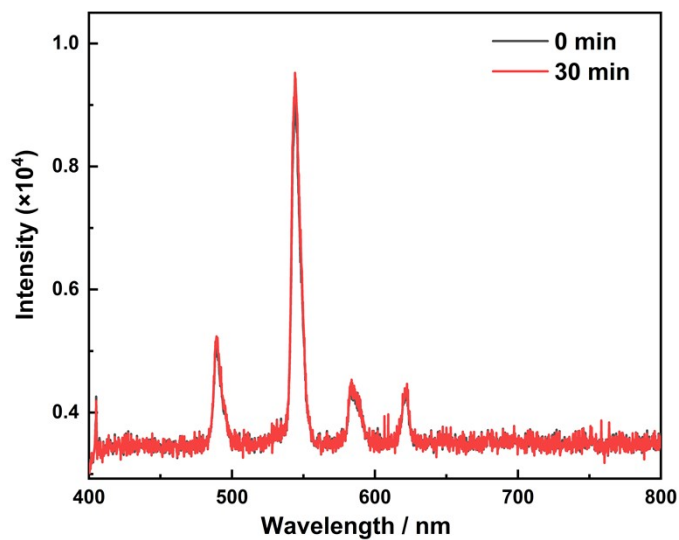
Figure S14. The spectrum of the solution (Tb^{3+} dissolved in DMF) reacted under plasma for 0 and 30 min, respectively.
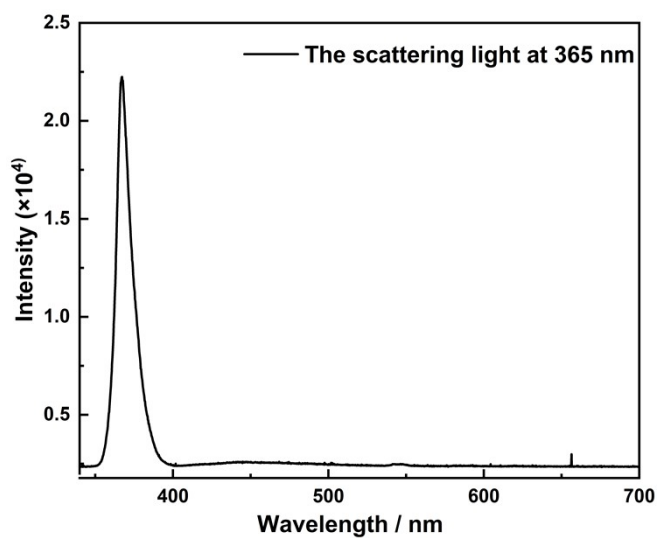

Figure S15. The scattering light at 365 nm. Notation: The 365 nm UV light instead of 302 nm UV light can also be scattered into the CCD detector when the solution become turbid.
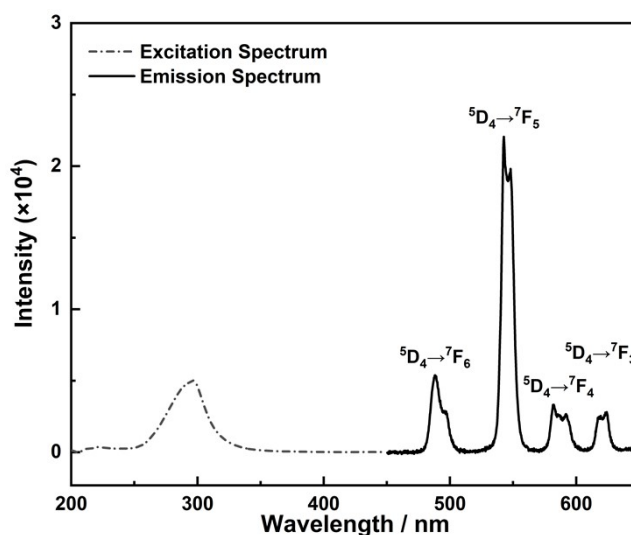
Figure S16. Fluorescence emission and excitation spectra of Tb(BTC). Notation: the light at 405 nm cannot be absorbed.

We built the *in-situ* transmission experimental device (Figure S17). Compared with the *in-situ* device shown in Figure 1, there is an additional 657 nm LED spotlight as a transmission light source, placing in the direction parallel to the CCD detector. When the reaction started, the LED and ultraviolet lamp were turned on, the scattering at 405 nm, the fluorescence between 450 ~ 650 nm, and the transmission light through the reaction medium at 657 nm were continuously and simultaneously measured by means of an optical fiber connected to a CCD detector. To explore the stability of the light source, DBD reactor loaded with DMF was applied as contrast experiment to monitor the blank intensity at 657 nm. As the blue line shown in Figure S18, the intensity of light source remained stable during the whole reaction, indicating there is no signal interference caused by the instability of the light source.

In order to explore the relationship between transmission light and scattering, the dependence of the intensity of the light on the reaction time was studied as shown in Figure S18 and the complex reaction process was divided into three different periods, namely I, II, III. In the period I, the intensity of scattering and the transmission light remained unchanged, indicating that no products formed in the solution. In the period II, the intensity of the transmission light strongly decreases, indicating the beginning of crystallization at this time, while the intensity of the scattering strongly increases. In the period III, the intensity of the transmission light reaches at this reaction stage its lowest values, caused by the turbidity of the solution blocking the light transmission, indicating the end of the reaction, while the intensity of scattering slowly decreased, then slowly rose and finally reached a plateau. The experimental results showed that the change of the scattering intensity was opposite to the change of the transmission intensity, which can sense the increase of the turbidity caused by the formation of solid materials, and reflect more information of process change.
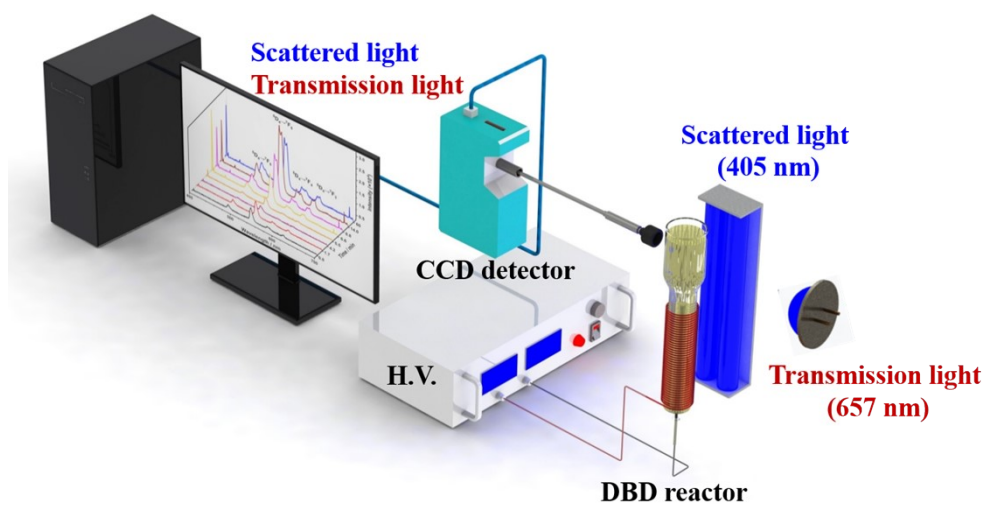
Figure S17. *In-situ* DBD-based reactor setup for monitoring the synthesis of materials applying time-resolved measurements of luminescence spectra and light transmission.
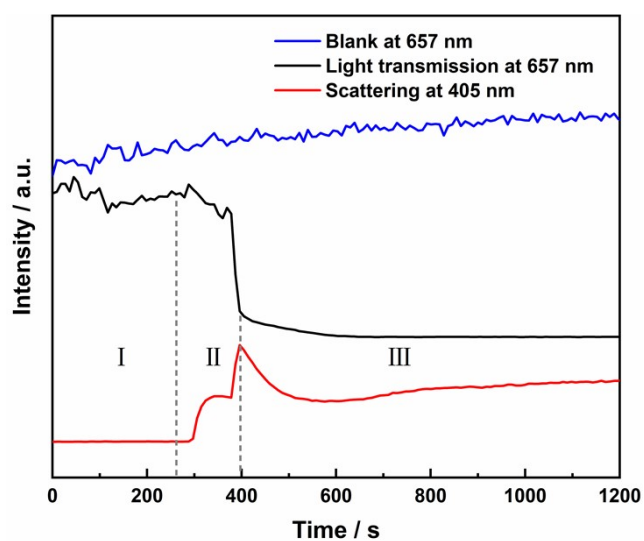

Figure S18. Light transmission detected at 657 nm through the reaction medium and scattering detected at 405 nm.
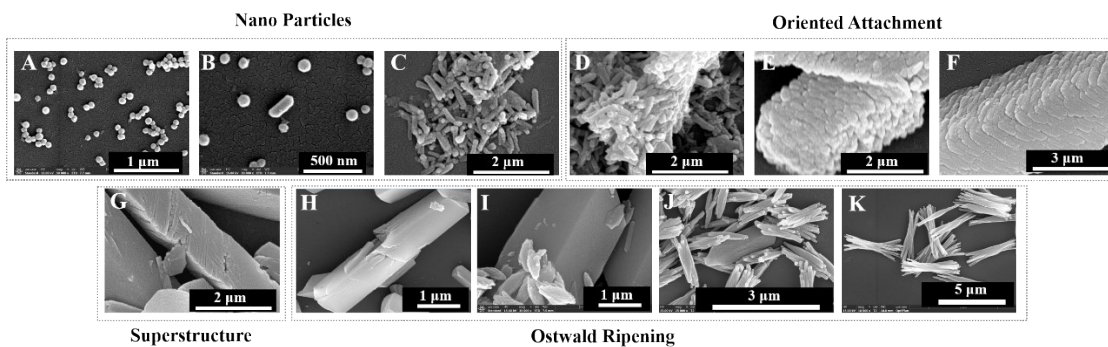
Figure S19. SEM micrographs of Tb(BTC) with different reaction time named Tb(BTC)-A, B, C…K. For Tb(BTC)-A, B, C: the nano-sized primary particles in period I; for Tb(BTC)-D, E, F, G, H: the bulk intermediates in period II; for Tb(BTC)-I: bulk intermediates and primary Tb(BTC) products coexist in period III; for Tb(BTC)-J: primary Tb(BTC) products in period IV; and for Tb(BTC)-K: Tb(BTC) products in period V.
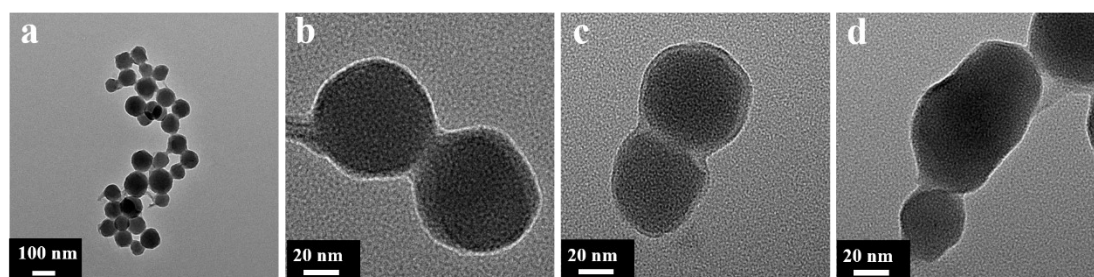

Figure S20. (a) TEM of the structure for Tb(BTC)-A. (b), (c) and (d) TEM of the structure for Tb(BTC)-B.
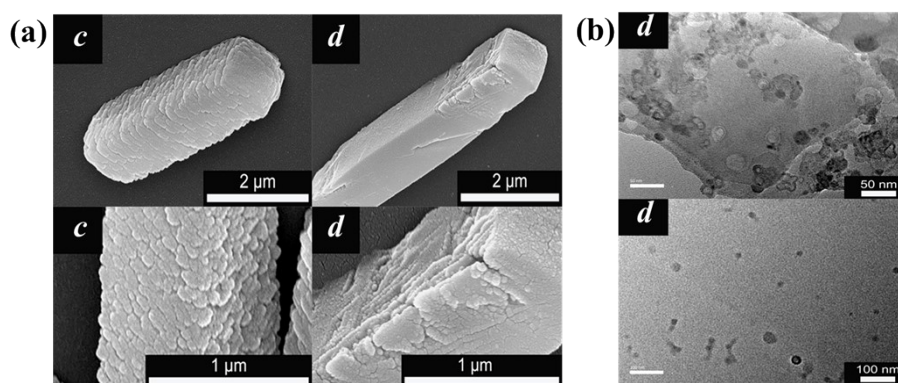

Figure S21. (a) SEM images of the surface view of Tb(BTC) at point c, d. (b) TEM images of these nanosized particles in the Tb(BTC) at point d.
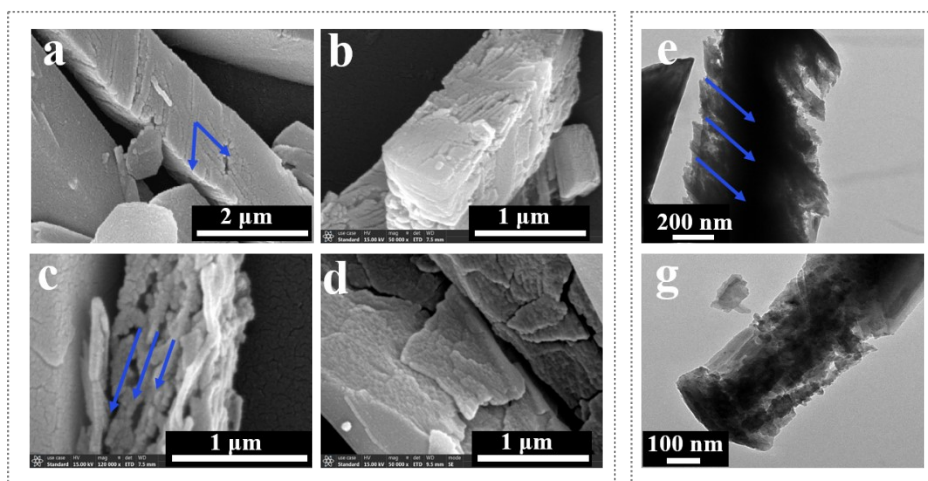
Figure S22. (a) and (b) SEM images of the front view of Tb(BTC)-G. Blue arrows show the angles of 60° between two stripes. (c) SEM of the broadside view for Tb(BTC)-G. (d) SEM of the truncated corner of crystals for Tb(BTC)-G. (f) TEM of the layer-by-layer structure for Tb(BTC)-G. (g) TEM of these nanosized particles in the Tb(BTC)-G.
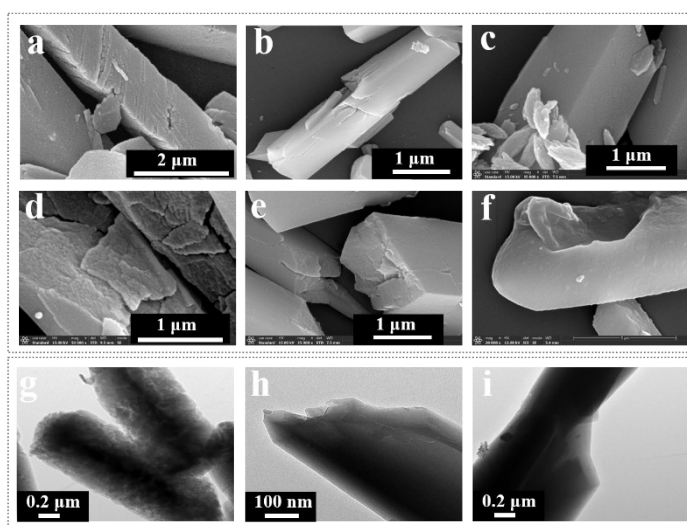

Figure S23. (a), (b) and (c): SEM images of the front view for Tb(BTC)-G, H, I, respectively. (d), (e) and (f): SEM images of the truncated corner of crystals for Tb(BTC)-G, H, I, respectively. (g), (h), and (i): TEM images for Tb(BTC)-G, H, I, respectively.
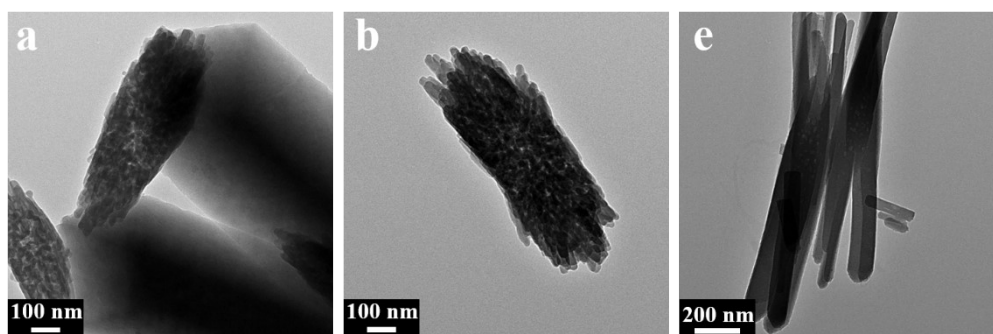
Figure S24. TEM images for Tb(BTC)-I, J, K.

The straw-sheaves Tb(BDC) are composed by short rigid nanorods, while the straw-sheaves Tb(BTC) are composed by elongated rigid nanorods, and the straw-sheaves Eu(BTC) are assembled by outspread and flexible nanobelts. Actually, these sheaf structures of the three materials may be formed by crystal splitting during their growth and crystal splitting often occurs in a crystal with structural anisotropy, which prefers 1D growth and has relatively small lateral adhesion energy.[4] The structure of Ln-BTC consists of 1D ribbon-like molecular motifs,[5] while Ln-BDC was 2-D sheetlike framework,[6] so the split amplitude of Ln(BTC) were more sharper than Ln(BDC). Kinetically, crystal splitting is associated with fast crystal growth, which depends strongly on the oversaturation of the solution.[7] The precursor solution of Eu(BTC) system was more prone to oversaturation than Tb(BTC) because of the different solubility of the two salts, which leads to a faster growth rate of Eu(BTC), so the split amplitude of Eu(BTC) was significantly larger than that of Tb(BTC).
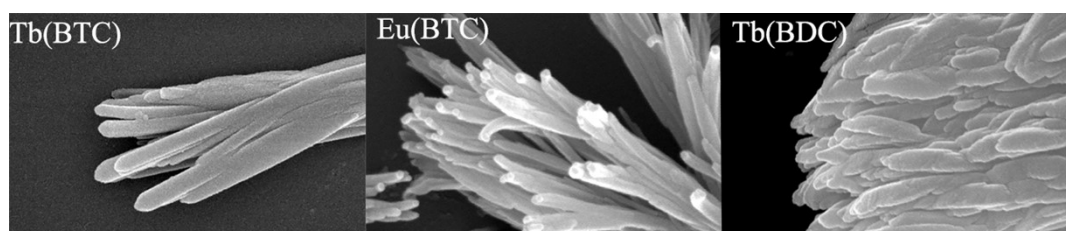

Figure S25. SEM images of three materials architectures.

Detection of formation of Tb(BDC) and Eu(BTC) by Scattering

For the Tb(BDC) synthesis system (Figure S26), the intensity of the scattering was continuous increased from period II to IV, and attenuation of scattering intensity is not observed as in the Tb(BTC) synthetic systems, indicating that no smaller products formed, which is also confirmed by SEM analysis. In the process of crystal growth, the Tb(BDC) was generated from nano-size particles to straw-sheaves via ion-by-ion

attachment. There were no bulk intermediate products and smaller products formed, which may be explained by classical growth process of Tb(BDC) crystallization.
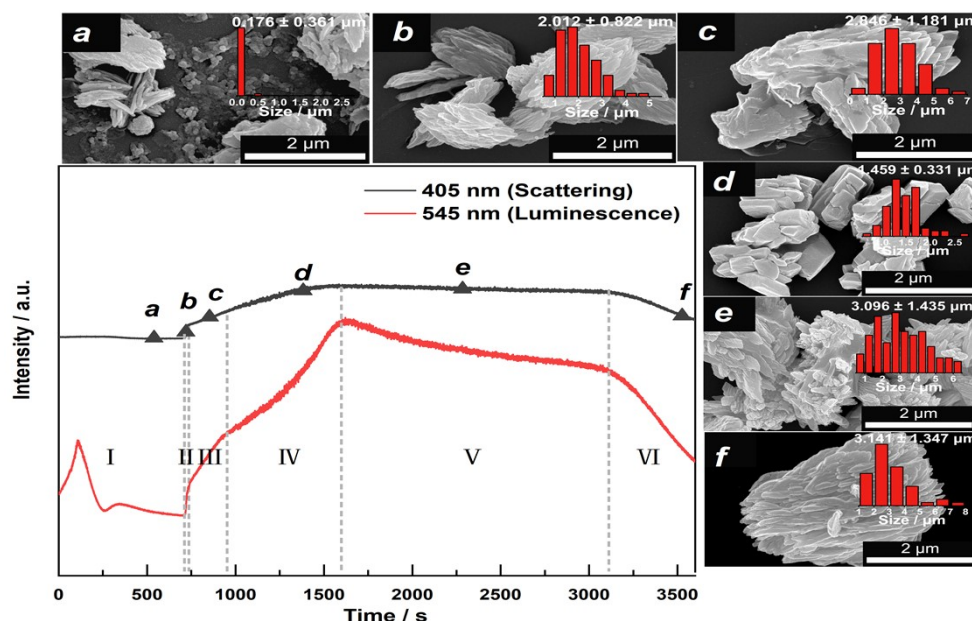

Figure S26. *In-situ* scattering measurements during the formation of Tb(BDC). Red bar graphs in (a-f) represent the size distribution of crystals. I: Nano-sized primary particles; II: Generation of products; III, IV: Growth of products; V: End of reaction; VI: Fragmentation of products.

For the Eu(BTC) synthesis system (Figure S27), the intermediate product of Eu(BTC) with aggregated large-size straw-like morphology was appeared in period II, which was different with Tb(BTC) intermediate constituted by nano-size particles (Figure 3). These phenomena can be explained by the different rate of crystal growth in period II (Figure S28a). The faster growth rate of Eu(BTC) compared with Tb(BTC), resulting in the crystal growth and orientation attachment occurred simultaneously. As the reaction continued, the large-size straw-like materials of Eu(BTC) disappeared at point d, the nano-size particles were generated by the broken straw-like materials at point e in period III (Figure S27), which may result in the decay of the scattering intensity.
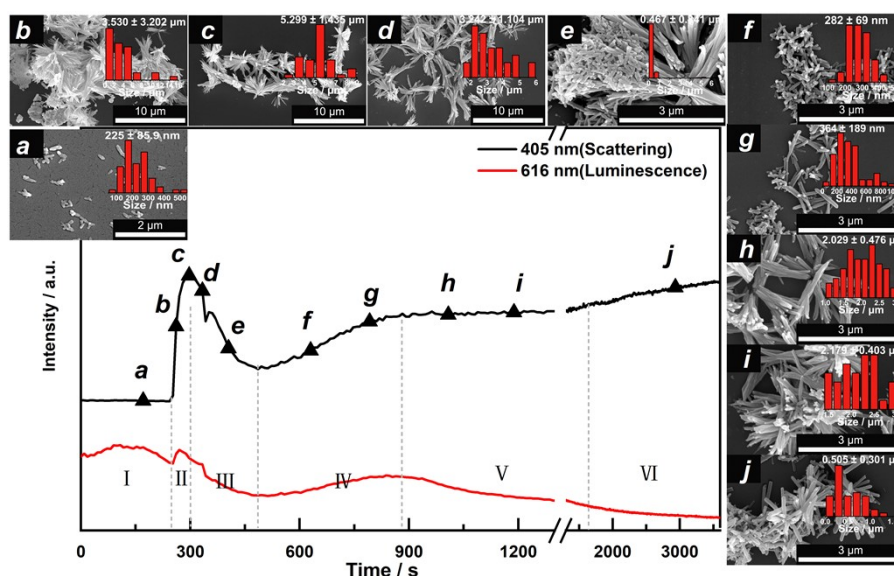
Figure S27. *Ex-situ* SEM measurements of Eu(BTC) at different points. Red bar graphs in (a-j) represent the size distribution of crystals. I: Nano-sized primary particles; II: Intermediates; III: Generation of products; IV: Growth of products; V: End of reaction; VI: Fragmentation of products.
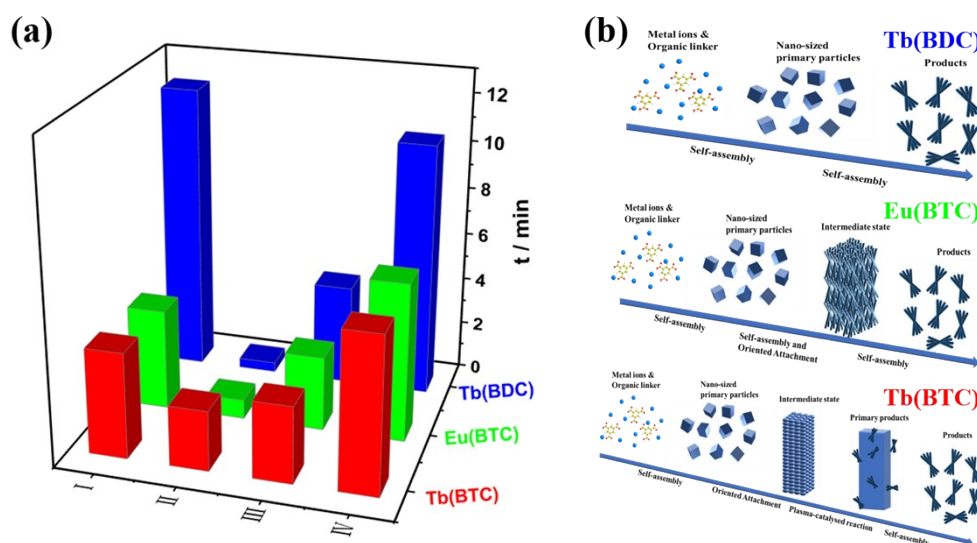

Figure S28. (a) The time required for different materials in different periods and (b) Schematic diagram of the pathway of crystal growth process for different materials under plasma-catalysed reaction.

The morphology and the size of porous materials are very important for applications such as catalysis,[8] adsorption,[9] and separation.[10] The temporal trend can roughly reflect the changes in the morphology and size of the material during the synthesis processes. Therefore, we collected the Tb(BTC) products in periods IV, V, and VI, respectively, to investigate the porosity of the products in different reaction period (Figure 29a). The BET surface area and micropore volume of Tb(BTC) were 557 m^2 g^{-1} and 0.37 cm^3 g^{-1} in period IV, 489 m^2 g^{-1} and 0.31 $cm^3 g^{-1}$ in period V and 457 m^2 g^{-1} and 0.29 cm^3 g^{-1} in

period VI, respectively, showing a sequentially decreasing trend. The surface area of the materials obtained in the earlier stage was maximized due to the small and homogeneous particles (1~2 μm), which is expected to be used as multifunctional materials on further investigations. Further extension of the synthesis time, however, led to a decrease in BET area (Figure 29b). The thermogravimetric (TG) curves of Tb(BTC) obtained from period VI showed a reduced thermal stability in comparison with samples obtained from earlier stages (Figure 29c). The flower-like products were broken in period VI (Figure 3). These observations can be explained by the accumulation of defects in the Tb(BTC) framework with long synthesis time under the plasma conditions.[11] Therefore, *in-situ* monitoring the synthesis of Tb(BTC) can provide useful guidance for maximizing surface area and framework stability.
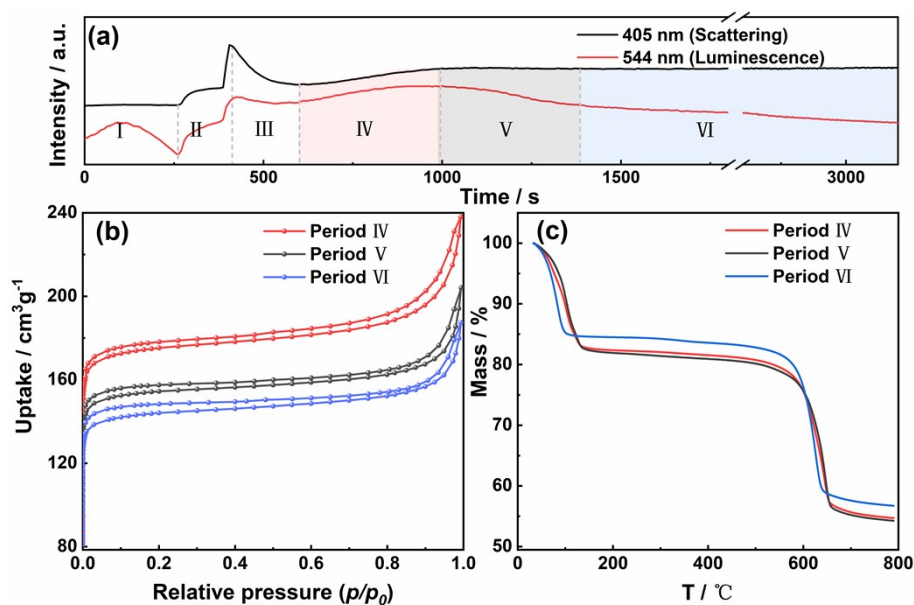

Figure S29. (a) Time dependence of emission and scattering intensity; (b) Nitrogen-adsorption isotherms of Tb(BTC); (c) TG curves of Tb(BTC).

References

1 N. L. Rosi, J. Kim, M. Eddaoudi, B. Chen, M. O'Keeffe and O. M. Yaghi, *J. Am. Chem. Soc.*, 2005, **127**, 1504-1518.

2 B. Chen, Y. Yang, F. Zapata, G. Lin, G. Qian and E. B. Lobkovsky, *Adv. Mater.*, 2007, **19**, 1693-1696.

3 T. M. Reineke, M. Eddaoudi, M. Fehr, D. Kelley and O. M. Yaghi, *J. Am. Chem. Soc.*, 1999, **121**, 1651-1657.

4 H. Deng, C. Liu, S. Yang, S. Xiao, Z.-K. Zhou and Q.-Q. Wang, *Cryst. Growth Des.*, 2008, **8**, 4432-4439.

5 Y. Zheng, K. Liu, X. Sun, R. Guan, H. Su, H. You and C. Qi, *CrystEngComm*, 2015, **17**, 2321-2326.

6 X.-P. Yang, R. A. Jones, J. H. Rivers and R. Pen-jen Lai, *Dalton. T.*, 2007, 3936-3942.

7 J. Tang and A. P. Alivisatos, *Nano Lett.*, 2006, **6**, 2701-2706.

8 D. Yang and B. C. Gates, *ACS Catal.*, 2019, **9**, 1779-1798.

9 H. E. Emam, R. M. Abdelhameed and H. B. Ahmed, *J. Environ. Chem. Eng.*, 2020, **8**, 104386.

10 X. Yang and Q. Xu, *Cryst. Growth Des.*, 2017, **17**, 1450-1455.

11 H. Embrechts, M. Kriesten, K. Hoffmann, W. Peukert, M. Hartmann and M. Distaso, *J. Phys. Chem. C*, 2018, **122**, 12267-12278.